ORIGINAL ARTICLE

Numerical analysis of the flow field in a planar nozzle for different divergent angles

S. L. Tolentino[1,2]*, J. Mírez[2], O. González[3]

[1] Faculty of Mechanical Engineering, National Experimental Polytechnic University "AJS" Vice-Rectorate (UNEXPO) Puerto Ordaz, Bolívar, Venezuela

[2] Group of Mathematical Modelling and Numerical Simulation (GMMNS), Faculty of Oil, Natural Gas and Petrochemical Engineering, Universidad Nacional de Ingeniería (UNI), Lima, Peru

[3] Faculty of Civil Engineering, National University Hermilio Valdizán (UNHEVAL), Huánuco, Perú

ABSTRACT – In the present work, the flow field is analysed for Mach number, pressure and temperature in 2D computational domains for a planar nozzle of symmetrical geometry as used in the experimental tests for cold flow. The study has been considered for $\alpha = 9°$, $\alpha = 11.01°$ and $\alpha = 13°$, and pressure ratios NPR = 2.412, NPR = 3.413, NPR = 5.423 and NPR = 8.78. For the numerical simulation of the turbulence in the presence of shock waves, the RANS model, the Sutherland equation and the Spalart-Allmaras turbulence model were used in the ANSYS-Fluent R16.2 code. The results obtained show fluctuations at the intersections of the internal shocks in the divergent, and the fluctuation decreases as the angle of the divergent increases. For NPR = 3.413, NPR = 5.423 and NPR = 8.78, the Mach number at the nozzle exit is the same, where for $\alpha = 11.01°$ Mach 2.00 was obtained, and based on this reference, for $\alpha = 13°$ there is an increase in velocity of 4.15% and for $\alpha = 9°$ a decrease in velocity of 3.78%. It also was found that the lowest pressure and temperature drop occurs at the nozzle outlet for $\alpha = 13°$.

INTRODUCTION

The flow field in supersonic nozzles for different geometries is studied recurrently. During the development of the flow regime, phenomena inherent to the nature of compressible flow occur. Depending on the pressure conditions in the flow field, the flow may be overexpanded, adapted or underexpanded [1]. When the flow is overexpanded, shock waves occur inside the nozzle, causing flow separation, detachment of the divergent wall boundary layer and recirculation of the flow adjacent to the wall after the shock, and depending on the geometry of the nozzle, side loads have significant effects caused by sudden pressure variations in the flow field [2-4]. In the central region of the diverging section of a high power supersonic nozzle, the flow decreases in temperature due to expansion, however, a region of the flow adjacent to the wall increases in temperature due to friction, which is higher than the central region of the flow. At the nozzle wall, the thermal effect is controlled by cooling systems [1, 2, 4]. While in low power nozzles that do not use cooling systems, for the overexpanded flow condition, the diverging walls reach high temperatures up to the shock wave position, after the shock, the temperature is much lower, so that the temperature differences present thermal effects due to the thermal expansion of the nozzle wall. The flow development in supersonic nozzles can be manipulated when it comes to experimental laboratory equipment for cold flow. A wide variety of experimental equipment is available for specific purposes for symmetric and asymmetric geometries, such as conical nozzles, planar nozzles, bell nozzles, nozzles with single and double divergent sections, nozzles with mechanical adaptations of flow deflection at the nozzle outlet, nozzles with additional flow injections to modify the flow path [1, 5-9], as well as transonic diffusers to decelerate the flow [10]. Nozzle designs are based on the half angle, α, of the diverging section, which is 12° to 18°, and the same principle applies to planar nozzles [1]. Nozzles with half angles less than 12° are classified as off-design nozzles.

It is called cold flow when the flow enters the experimental apparatus at room temperature, and is denoted hot flow when the flow enters at high temperature, as in the case of rocket engine nozzles. It should be noted that the temperature gradients for hot and cold flow in the central region of the flow are different from each other, as well as the thermal effect on the walls of supersonic nozzles. In experimental nozzles, flow turbulence and shock waves can be physically reproduced in the laboratory, and images can be captured with the Schlieren technique [11] of the shock wave form structures, the region where the internal shock occurs, oblique shocks, reflected shocks and the shock front known as the Mach disk [1, 2, 12]. The Schlieren technique consists of capturing images through an optical process of the shadows produced by the density variation of a fluid, and was proposed by the German physicist August Toepler in 1864 [11], which allows the identification of critical regions where the flow presents unusual patterns, and these critical regions are the focus of interest for researchers to study. Using the Schlieren technique it is not possible to determine the magnitudes of the thermodynamic parameters of the flow field, so computational fluid dynamics (CFD) codes using governing equations and turbulence models [14] are used to simulate the turbulence of the flow in the presence of shock waves, and so, it is able to determined those magnitudes.

Within the diversity of experimental equipment for supersonic flow, this research has focused on the study of cold flow behaviour in planar nozzles. Hunter [5] performed experimental tests and numerical simulations for overexpanded

and underexpanded cold flow for an off-design planar nozzle, who reported experimental pressure patterns evaluated at the nozzle wall, as well as images of shock waveforms captured with the Schlieren technique. As the flow pressure load at the nozzle inlet increases, shock waves begin to appear in the divergent with progressive changes in their structure; as well as, changes in the position of the oblique shocks, reflected shocks and Mach disk. It also has been observed that the onset of the formation of the internal shock that defines a pattern of crossed diagonals as the shock front moves towards the nozzle exit, the region where the flow separation starts, the recirculation of the flow after the oblique shock, and the turbulence after the shock at the ends of the Mach disk. It should be noted that, depending on the aerodynamic profile of the nozzle wall and the flow pressure ratio, after the shock, the flow separation is classified as restricted shock separation (RSS) when the flow separates and downstream re-attaches to the wall, forming a bubble between the separation and re-attachment; and free shock separation (FSS) is when downstream there is no re-attachment of the flow to the wall [2].

The experimental data reported by Hunter [5] were used by different researchers to validate turbulence models and analyse the turbulence in the flow field [15, 16], to analyse the imposed oscillation conditions [17], to study the symmetry and asymmetry of the flow [18], as well as to study the flow in walls with porous surfaces [19]. Other experimental studies of the flow field for planar nozzles with different geoemetries were reported in the literature, such as the study of low Mach number flow [20], influence of wall roughness on flow asymmetry [21], flow asymmetry at low pressure ratios [22], flow asymmetry for $\alpha < 11°$ [23], flow behaviour in a double divergent planar nozzle [24], flow turbulence in a vector planar nozzle [25], and the effect of hysteresis in a stepped planar nozzle [26]. To model the turbulence of the flow field, CFD computational tools have a great potential to reproduce the flow turbulence, which allows to quantify the thermodynamic parameters of pressure, temperature, Mach number, among other parameters. Therefore, different investigations on turbulence flow in planar nozzles applying CFD reported approximate solutions and were compared with experimental data, which were reported in [5, 8, 15, 16, 25, 27].

In the present work, the objective is to analyse the flow field for Mach number, static pressure and static temperature, for the symmetric geometry of an experimental planar nozzle for cold flow, and whose planar nozzle corresponds to the work reported by Hunter [5]. The geometry of the planar nozzle is considered for $\alpha = 9°$, $\alpha = 11.01°$ and $\alpha = 13°$. The flow pressures at the nozzle inlet are considered for four cases of pressure ratio: NPR = 2.412, NPR = 3.413, NPR = 5.423 and NPR = 8.78. To achieve the proposed objective, the turbulence of the flow field is simulated with the ANSYS-Fluent R16.2 code for nine 2D computational domains, where the domain is discretised by the finite volume method (FVM). In the materials and methods section, the experimental planar nozzle, the computational domain, the governing equations, the numerical convergence analysis, the computational solution method and the validation of the turbulence model used are presented. In the results and discussion section, the flow field and the patterns of velocity, pressure and temperature are analyzed. Afterward the conclusions are presented.

MATERIALS AND METHODS

Planar Nozzle and Computational Domain

The experimental planar nozzle [5] considered for the study of cold flow in the present work is illustrated in Figure 1, which is used to perform experimental tests for compressible flow at high velocities. The experimental equipment belongs to NASA Langley Research Center 16-Foot Transonic Tunnel Complex [5]. The fundamental characteristics of the planar nozzle are the throat cross-sectional area $A_t = 2785.1557$ mm^2 (4.317 pulg^2); the expansion ratio $A_e/A_t = 1.797$, where A_e is the area at the nozzle outlet; as well as, the planar nozzle width of 101.346 mm (3.99 pulg). Furthermore, based on the one-dimensional theory, the nozzle was designed for the pressure ratio NPR = 8.78 and Mach number 2.07 at the nozzle outlet; and for the ambient pressure $P_{amb} = 102.387$ kPa (14.85 psi). The high-pressure air flow is semi-injected into the nozzle with stagnation temperature control at 294.444 K (530 R), and mass flow up to the capacity of 6.804 kg/s (15 lbm/sec). It should be noted that all geometrical parameters and flow data for the experimental planar nozzle are reported in the work of Hunter [5]. The geometry of the planar nozzle was considered for $\alpha = 9°$, $\alpha = 11.01°$ and $\alpha = 13°$. Where $\alpha = 11.01°$ corresponds to the original design of the planar nozzle from Hunter's work [5], and the angles $\alpha = 9°$ and $\alpha = 13°$ are part of the adaptation of the geometry by the authors of the present work.

Due to the symmetry of the planar nozzle, a 2D domain was considered, as shown in Figure 2(a). The 2D domain includes a short section at the inlet of the nozzle to direct the flow, a section for the flow discharging to the atmosphere, as well as, the boundary conditions are indicated in the domain. The Figure 2(b) shows the third meshed domain, Mesh 3, with a mesh structure of 29160 elements; and enlarged details of the refined mesh in the wall region of the throat section and the wall corner at the nozzle outlet (Figures 2(c) and 2(d)). The third meshed domain of the nozzle is illustrated in Figure 2(b) and corresponds to $\alpha = 11.01°$, but the domains and meshes for $\alpha = 9°$ and $\alpha = 13°$ are not presented, as they are similar. For the meshing in the corner wall region of the nozzle, a different meshing technology than the traditional one was applied. The corner region was divided into several subdomains to control the distribution of cells in the vertical and horizontal direction. In this way, an unnecessary increase of cells leading to cross-crowding at the corners and higher computational cost during iterations was avoided.
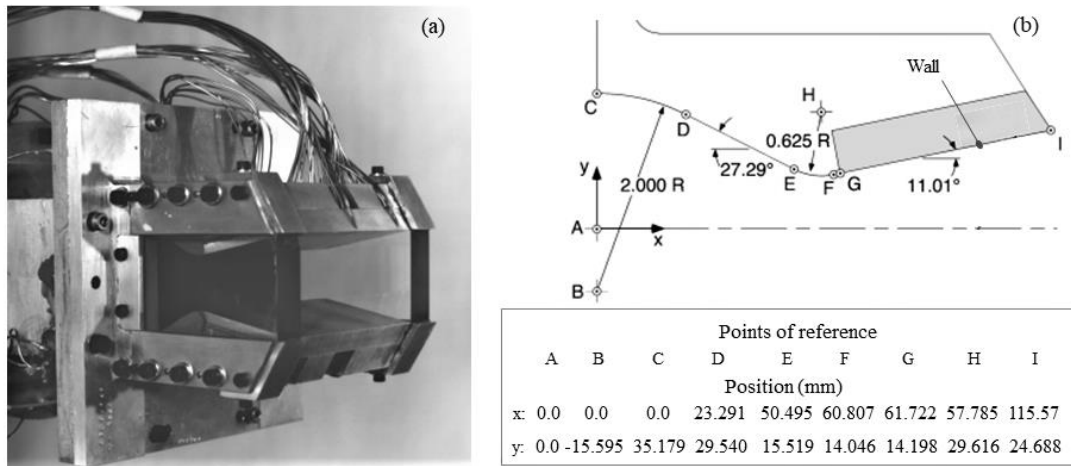
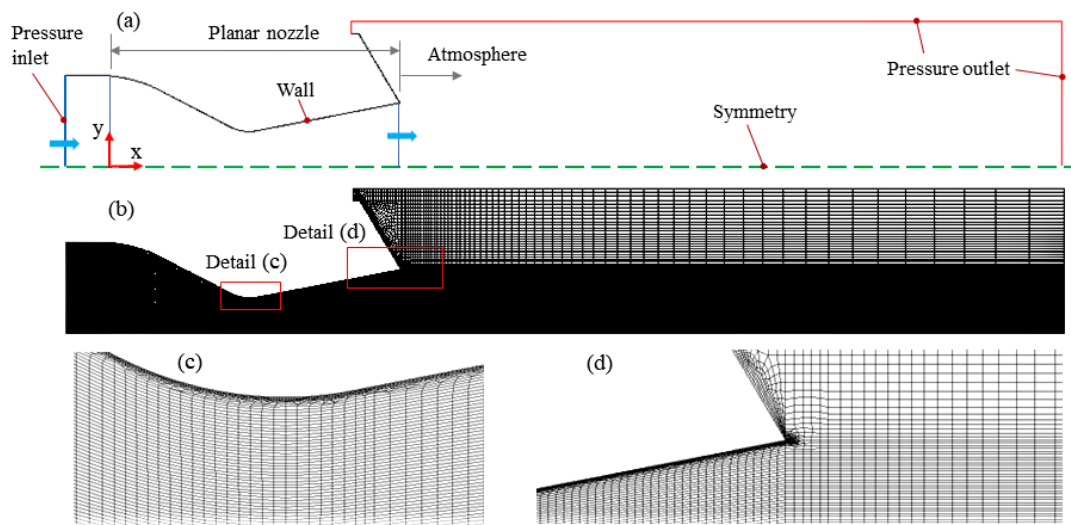**Figure 1.** (a) Experimental planar nozzle and (b) Schematic and dimensions [5]

Figure 2. (a) Computational domain; (b) Third meshed domain, Mesh 3, with 29160 elements, for α = 11.01°; (c) Magnified detail of the throat section and (d) Magnified detail of the corner section

The flow used in the experimental planar nozzle is air, which has been considered as an ideal gas. The specific heat ratio $k = 1.4$, the gas constant $R = 287$ J/(kg · K) the specific heat at constant pressure $C_p = 1006.43$ J/(kg · K) and the thermal conductivity $k = 0.0242$ W/(m · K) [28]. The initial and boundary conditions were set as: in the atmosphere the pressure $p = p_{atm} = 102.387$ kPa and the temperature $T = T_{atm} = 294.444$ K. The flow at the nozzle inlet was considered for four cases of total pressure, $p_o = p_{ent}$, where p_o/p = NPR. Where the pressure ratios are: NPR = 2.412, NPR = 3.413, NPR = 5.423 and NPR = 8.78, for the planar nozzle with $\alpha = 9°$, $\alpha = 11.01°$ y $\alpha = 13°$. The total temperature at the inlet of the nozzle was set with constant value $T_o = T_{ent} = 294.444$ K. In the adiabatic wall, the flow velocity is zero due to the no-slip condition. In the symmetry, in the y-axis direction the velocity is zero. The effect of gravity on the nozzle section and the atmosphere is not taken into account since a 2D domain with symmetry in the y-axis direction is considered. It should be noted that the pressure and temperature data were taken from the work of Hunter [5].

Mathematical Fundamentals

In the present work, for the flow field simulations with the ANSYS-Fluent R16.2 code, the model of the steady-state flow Reynolds-Averaged Navier-Stokes (RANS) equations is used. The four governing equations are: the equation of conservation of mass Eq. (1), momentum Eq. (2), energy Eq. (3), and the ideal gas Eq. (4) [28]; which, in compact form are expressed as:

$$\nabla \cdot (\rho u_i) = 0 \tag{1}$$

where ρ is the density and u is the velocity.

$$\nabla.\left(\rho u_i u_j\right) = -\nabla p + \nabla.\left(\bar{\bar{\tau}}\right) + \nabla.\left(-\rho \overline{u_i' u_j'}\right) \tag{2}$$

where p is the pressure, $\bar{\bar{\tau}}$ is the stress tensor, y $-\rho \overline{u_i' u_j'}$ is the Reynolds stresses.

$$\nabla.\left(u_i(\rho E + p)\right) = \nabla.\left(k_{eff}\nabla T + \left(\bar{\bar{\tau}}_{eff}.u_i\right)\right) \tag{3}$$

where E is the total energy, T is the temperature, k_{eff} is the effective thermal conductivity, and $\bar{\bar{\tau}}_{eff}$ is the effective stress tensor.

$$p = \rho R T \tag{4}$$

It should be noted that the ANSYS-Fluent R16.2 code takes into account the density expressed as $\rho = (p_{op} + p)/(RT/M_w)$. Where p_{op} is the operating pressure, p is the local static pressure relative to the operating pressure, R is the universal gas constant and M_w is the molecular weight. The operating pressure, p_{op}, is a condition of the ANSYS-Fluent code itself, and is taken into account when applying the boundary conditions in the computational domain, $p_{op} = 0$ [28].

Other equations involved for compressible flow are the pressure ratio, Eq. (5) and the temperature ratio, Eq. (6) [28], which are expressed as follows:

$$\frac{p_0}{p} = \left(1 + \frac{k-1}{2}M^2\right)^{\frac{k}{k-1}} \tag{5}$$

$$\frac{T_0}{T} = 1 + \frac{(k-1)}{2}M^2 \tag{6}$$

where, p_0 is the total pressure, T_0 is the total temperature, M is the Mach number, and k is the ratio of specific heats.

For compressible flow, the dominant parameter is the Mach number. Mach number considerations are as follows: for incompressible flow $M < 0.3$; subsonic flow $0.3 \leq M \leq 0.8$; transonic flow $0.8 \leq M \leq 1.2$; supersonic flow $1,2 \leq M \leq 5$; hypersonic flow $M > 5$; sonic flow $M = 1$ [4].

Computational Solution Method

In the ANSYS-Fluent R16.2 code, different options were considered: In Solver, the following considerations were taken: Type: density-based; Time: steady; Velocity formulation: absolute; 2D space: planar. The Spalart-Allmaras S-A turbulence model [29] was considered. For the viscosity as a function of temperature the Sutherland equation [30]. For the solution method, the implicit formulation and Roe-FDS flow type were considered. For the spatial discretisation, the gradient: Least Squares Cell Based. For the flow, the kinetic energy turbulence and for the specific dissipation, the Second Order Upwind option was selected. For the mass balance control, mass flow rate was taken into account, for the error in the range of 1E-04 to 1E-06. The hybrid initialisation method was applied. From 3E+04 to 3.5E+04 iterations were performed to obtain the final results of the Mach number, pressure and temperature flow field. A computer with the following characteristics was used for data processing: Dell CPU, Optiplex 7010 model, i5 3470, four 3.2 GHz processors and 8 GB of RAM memory.

Numerical Convergence Analysis

The domains were meshed three times in the ANSYS-Meshing platform: the first meshed domain, mesh 1, with 27893 elements, the second meshed domain, mesh 2, with 28493 elements and the third meshed domain, mesh 3, with 29160 elements. The flow turbulence was evaluated with the Spalart-Allmaras S-A turbulence model [29], for NPR = 3.413 and NPR = 8.78. For the numerical convergence study, the Mach number at the nozzle outlet was obtained, for the Mesh 1, the Mach number 2.00155 was obtained for NPR = 3.413 and Mach number 2.00067 for NPR = 8.78. For the mesh 2, Mach number 2.00154 for NPR = 3.413 and Mach number 2.00074 for NPR = 8.78 were obtained. For the mesh 3, Mach number 2.0016 for NPR = 3.413 and Mach number 2.00082 for NPR = 8.78 were obtained. The six numerical results are close to the theoretical value of Mach number 2.07 for the planar nozzle design [5], for quasi-one-dimensional flow. It should be noted that for the flow field simulations, the mesh 3 with 29160 elements was taken into account, where for the Mach number, the absolute error is 0.068 for NPR = 3.413 and the absolute error is 0.069 for NPR = 8.78.
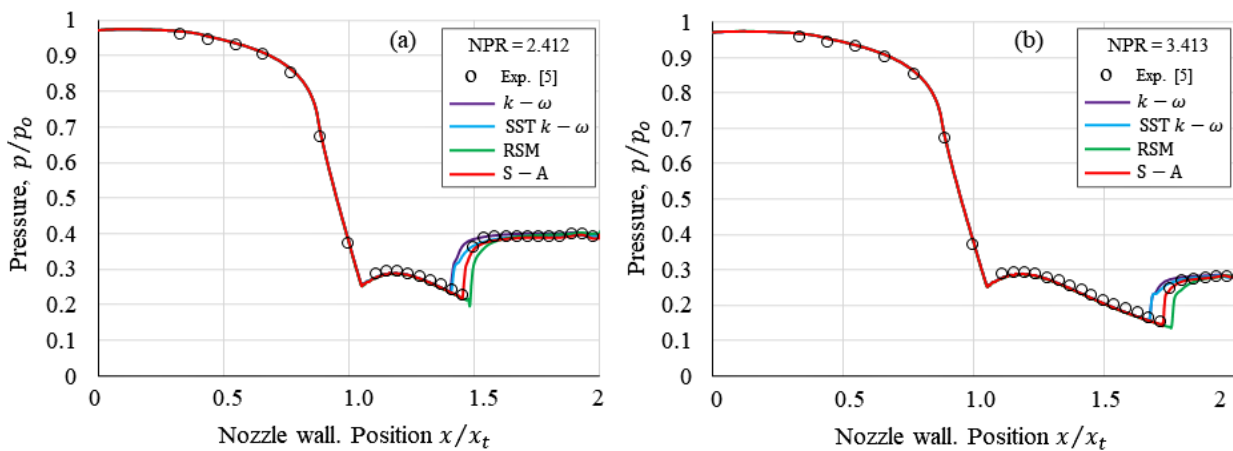
Figure 3(a) shows the pressure profiles at the nozzle wall for NPR = 3.413 and NPR = 8.78, for the three mesh domains: mesh 1, mesh 2 and mesh 3, which overlap. Figure 3(b) shows the profiles obtained at the otber wall for y^+, and it is observed that y^+ has higher values for NPR = 8.78, and this is because the mass flux is higher with respect to NPR = 3.413. The maximum peak of y^+ occurs at the entrance of the throat section for NPR = 3.413 and NPR = 8.78, close to $x/x_t = 0.9$, where the nozzle throat is located at position $x/x_t = 1$. For NPR = 3.413, y^+ decreases after flow separation, for the estimated position $x/x_t = 1.7$ until the nozzle exit which ends at position $x/x_t = 2$.
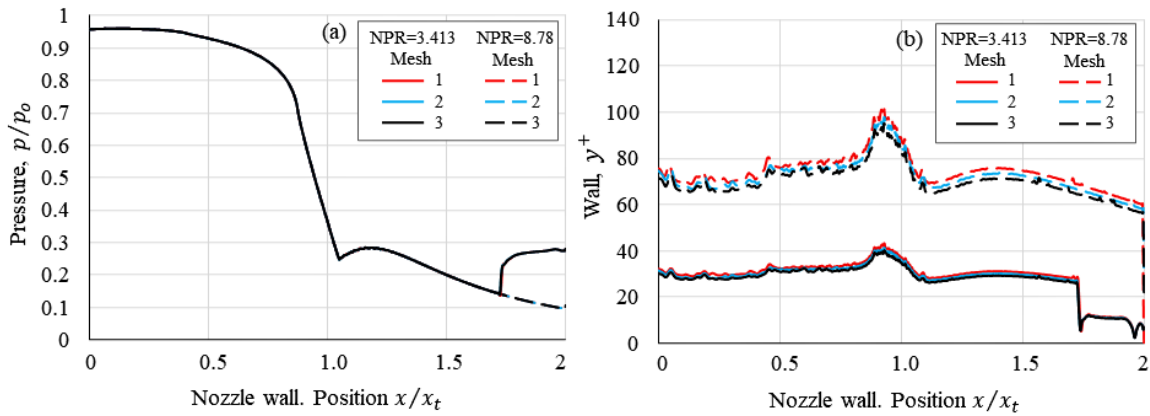
Figure 3. Behaviour of (a) pressure and (b) y$^+$ at the nozzle wall for three meshed domains, for NPR = 3.413 and NPR = 8.78

Validation of the Spalart-Allmaras Turbulence Model

The Spalart-Allmaras [29] S-A turbulence model was validated with the experimental pressure data reported by Hunter [5] for NPR = 2.412 and NPR = 3.413; also, the S-A model was compared with the standard $k - \omega$ turbulence models of Wilcox [31], SST $k - \omega$ of Menter [32] and RSM of Launder et al. [33]. The behaviour of the curve trajectories is shown in Figure 4(a) and 4(b), and it is observed that the S-A model curve has a better fit in the region where the lowest pressure drop occurs with respect to the experimental pressure data [5]. It should be noted that in the computational simulations for the validation phase, all four turbulence models were used without modifying their constant magnitude parameters. The S-A turbulence model is a single-equation model, and the profile trajectory shows that it has a better response to adverse pressure gradients and boundary layer separation than the other three turbulence models employed. The pressure data presented in Figure 4 were obtained at the walls of the planar nozzle shown in Figure 5, the same figure shows the structures of the shock waves captured with the Schlieren technique [5], Figure 5(a) for NPR = 2.412 and Figure 5(b) for NPR = 3.413.

Figure 4. Comparison of the pressure profiles of the simulations and the experimental pressure data, evaluated at the nozzle wall: (a) NPR = 2.412 and (b) NPR = 3.413
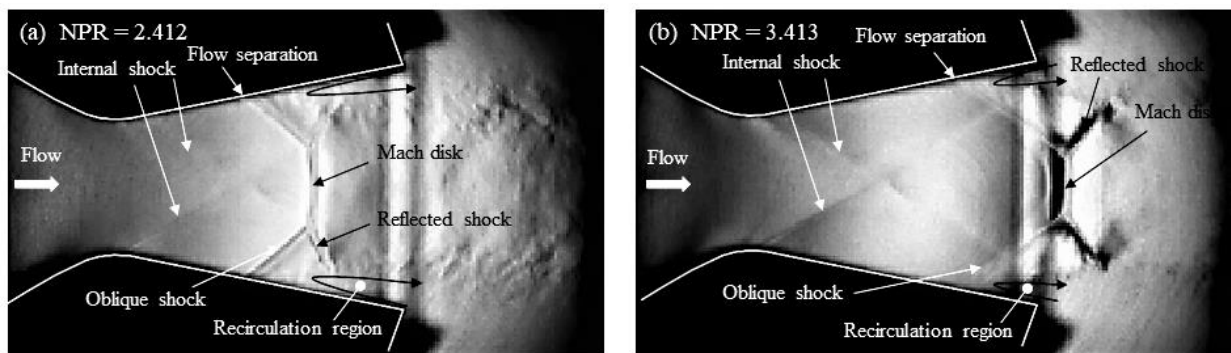
Figure 5. Shock waves in the experimental planar nozzle captured with the Schlieren technique [5]: (a) NPR = 2.412 and (b) NPR = 3.413

RESULTS AND DISCUSSION

This section presents the results obtained from the numerical simulations for the flow field for Mach number, static pressure and static temperature. Where the colour shading indicates for the blue colour the regions that present lower magnitude and the red colour indicates the regions that present higher magnitude, in the flow fields.

Flow Field: Mach Number

The flow field for Mach number is shown in Figures 6(a), 6(b) and 6(c). For NPR = 2.412, the flow is overexpanded and the shock wave is inside the nozzle, for NPR = 3.413 the shock front is outside the nozzle, but the oblique shocks are inside the nozzle. For NPR = 5.423 the shock wave is in the region of the atmosphere, and for NPR = 8.78 the flow is overexpanded. For NPR = 2.412 and $\alpha = 9°$, in the region of the atmosphere the supersonic jet is present in the central region, for $\alpha = 11.01°$ it separates slightly due to expansion, and for $\alpha = 13°$ the expansion is larger. The same happens when increasing for NPR = 3.413, NPR = 5.423 and NPR = 8.78. The distributions of the Mach number gradients are observed throughout the flow field, which define the shock wave structures in the nozzle and in the atmosphere.

Figures 7(a), 7(b) and 7(c) show the Mach number patterns that were evaluated in the planar nozzle symmetry. For the shock wave occurring inside the nozzle for NPR = 2.412, it is observed that for $\alpha = 9°$ the shock position is located at $x/x_t = 1.74$ and reaches Mach number 1.77, for $\alpha = 11.01°$ the shock position is located at $x/x_t = 1.7$ and Mach number 1.85, as well as, for $\alpha = 13°$ the shock position is located at $x/x_t = 1.67$ and Mach number 1.97. It is evident that by increasing α, inside the nozzle the flow expands and increases its acceleration, as well as, the position of the shock shifts towards the interior of the nozzle. At the nozzle exit at position $x/x_t = 2$, for NPR = 3.413, NPR = 5.423 and NPR = 8.78, for $\alpha = 9°$ the flow reaches the supersonic speed of Mach number 1.925, for $\alpha = 11.01°$ the Mach number 2.0008, and for $\alpha = 13°$ the Mach number 2.084. Therefore, the approximate solution of the flow velocity at the exit of the nozzle with respect to $\alpha = 11.01°$ which is taken as reference data, for $\alpha = 13°$ there is a velocity increase of 4.15%, and for $\alpha = 9°$ a velocity decrease of 3.78%. In the region of the atmosphere, for NPR=8.78, the maximum peak of Mach number 2.47 occurs for $\alpha = 9°$ and the maximum peak of Mach number 2.55 occurs for $\alpha = 13°$.
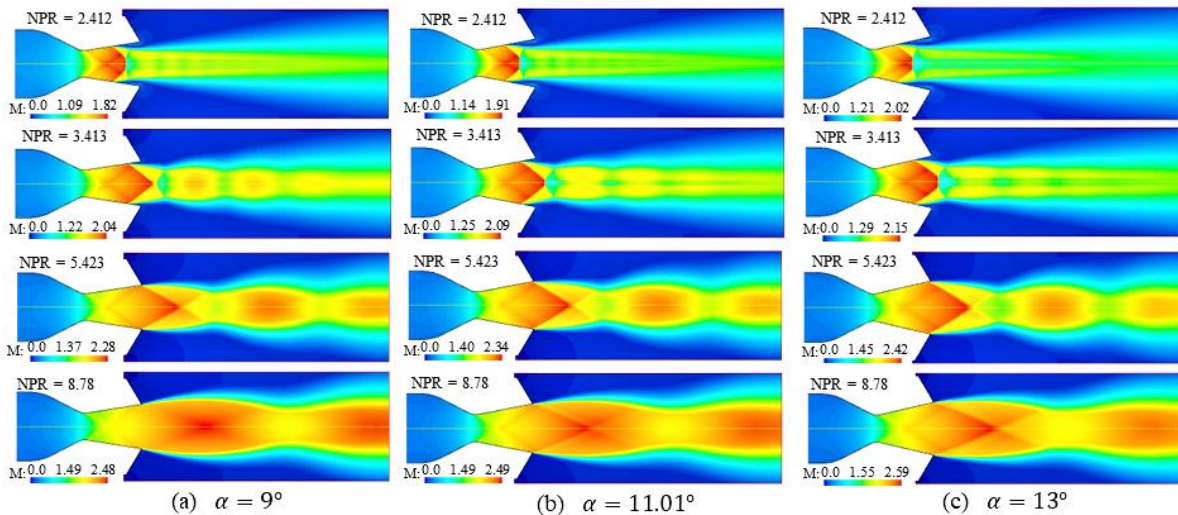

Figure 6. Flow field: Mach number, for (a) $\boldsymbol{\alpha = 9°}$, (b) $\boldsymbol{\alpha = 11.01°}$ and (c) $\boldsymbol{\alpha = 13°}$
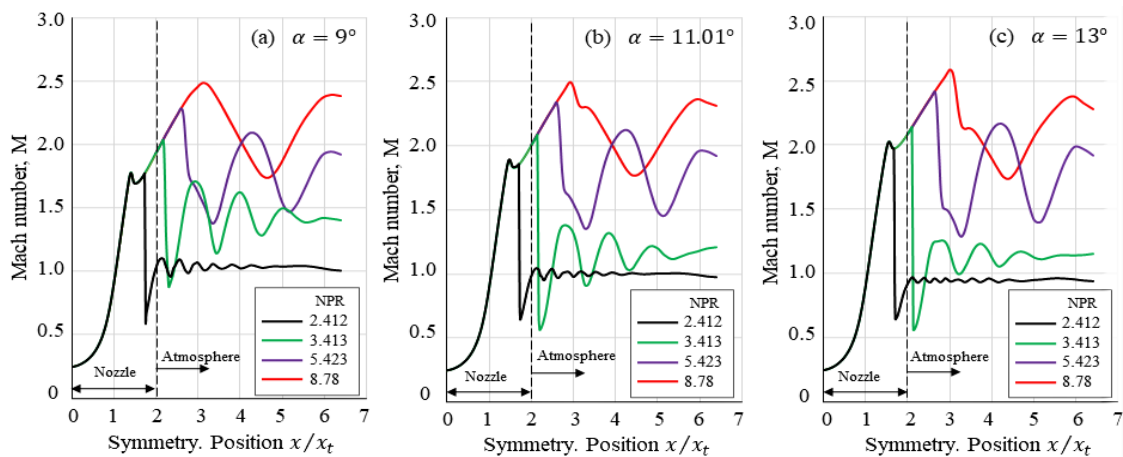
Figure 7. Mach number patterns in symmetry, for (a) $\boldsymbol{\alpha = 9°}$, (b) $\boldsymbol{\alpha = 11.01°}$ and (c) $\boldsymbol{\alpha = 13°}$
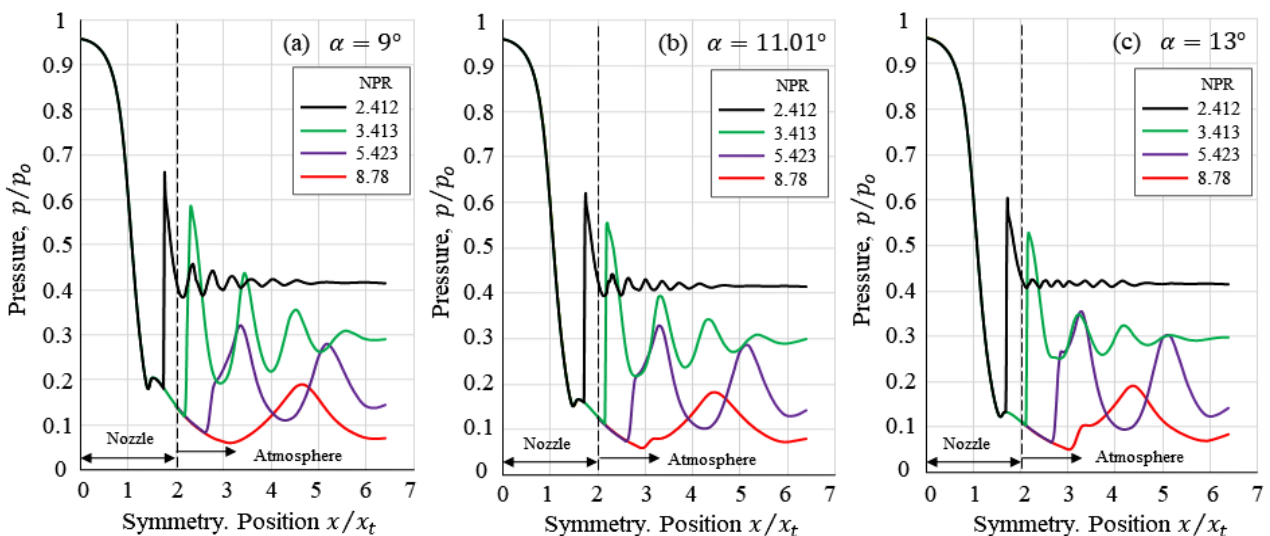
Flow Field: Static Pressure

The static pressure field is shown in Figures 8(a), 8(b) and 8(c). The pressure gradients are distributed throughout the flow field, and are observed to vary in the regions where shock waves are present. The flow for NPR = 3.413, the shock wave occurs inside the nozzle. For NPR = 3.413, as the flow velocity increases, the pressure decreases, and as the flow velocity decreases, the pressure increases. Therefore, pressure fluctuations are present in the supersonic jet in the nozzle and in the atmosphere, with greater intensity than for the flow with NPR = 2.412. The pressure gradients for NPR = 5.423 are higher at the exit of the nozzle, in the region where the shock wave is produced.

For NPR = 8.78, the pressure gradients in the internal shocks define well-defined structures, and in the atmosphere region the lowest pressure drops occur for NPR = 2.412, NPR = 3.413 and NPR = 5.423. The static pressure patterns evaluated in the planar nozzle symmetry are shown in Figures 9(a), 9(b) and 9(c). The behaviour of the curve trajectories in the nozzle and in the atmosphere is observed for $\alpha = 9°$, $\alpha = 11.01°$ and $\alpha = 13°$. For the shock wave that occurs inside the nozzle for NPR = 2.412, it is observed that for $\alpha = 9°$ the shock position is located at $x/x_t = 1.74$ and with a pressure drop $p/p_o = 0.18$; for $\alpha = 11.01°$ the shock position is located at $x/x_t = 1.7$ and with a pressure drop $p/p_o = 0.159$; as well as, for $\alpha = 13°$ the shock position is located at $x/x_t = 1.67$ and with a pressure drop $p/p_o = 0.133$. Therefore, the increase of α allows an increase of the pressure drop of the flow inside the nozzle. At the nozzle outlet at position $x/x_t = 2$, for NPR = 3.413, NPR = 5.423 and NPR = 8.78, for $\alpha = 9°$ the flow reaches a pressure drop $p/p_o = 0.143$, for $\alpha = 11.01°$ the pressure drop $p/p_o = 0.127$, and for $\alpha = 13°$ the pressure drop $p/p_o = 0.112$.
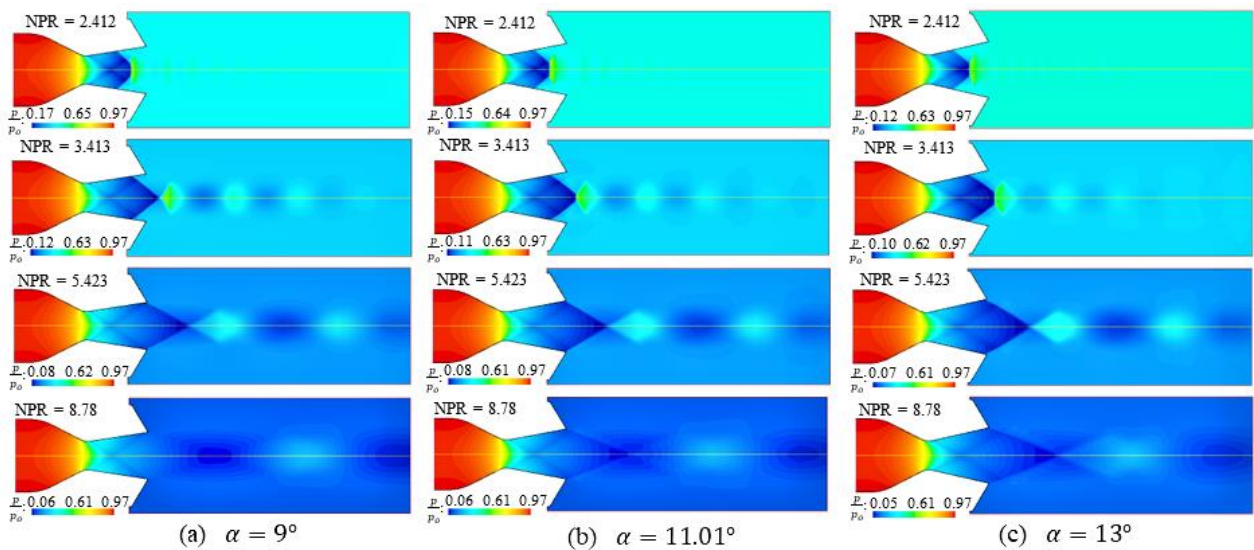
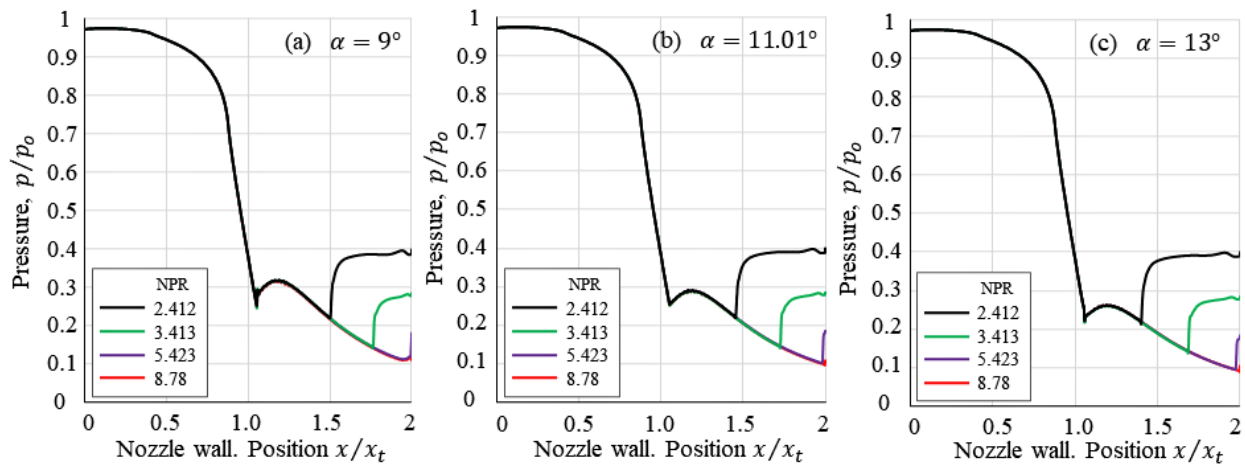**Figure 8.** Flow field: static pressure, for (a) $\boldsymbol{\alpha = 9°}$, (b) $\boldsymbol{\alpha = 11.01°}$ and (c) $\boldsymbol{\alpha = 13°}$

Figure 9. Static pressure patterns in symmetry, for (a) $\boldsymbol{\alpha = 9°}$, (b) $\boldsymbol{\alpha = 11.01°}$ and (c) $\boldsymbol{\alpha = 13°}$

As the nozzle is planar and the flow conditions are symmetrical in the 2D plane, the pressure distributions are the same on the top and bottom wall. The static pressure patterns at the nozzle wall are shown in Figures 10(a), 10(b) and 10(c). At the onset of flow separation, for $\alpha = 9°$ and NPR $= 2.412$ the pressure drop $p/p_o = 0.218$ is at position $x/x_t = 1.496$; for $\alpha = 11.01°$ one has $p/p_o = 0.216$ and $x/x_t = 1.450$; and for $\alpha = 13°$ we have $p/p_o = 0.212$ and $x/x_t = 1.397$; it is observed that as α increases the position of the flow separation shifts towards the inside of the nozzle. The same happens for NPR $= 3.413$ and NPR $= 5.423$. While for NPR $= 8.78$ the pressure drop occurs at the nozzle outlet, being the flow conditions undersized. Furthermore, it is observed in the throat region, at the estimated position around $x/x_t = 1.185$ a concave curve trajectory is presented, for $\alpha = 9°$ the dome is located at $p/p_o = 0.317$, for $\alpha = 11.01°$ at $x/x_t = 1.162$ and $p/p_o = 0.288$, and for $\alpha = 13°$ at $x/x_t = 1.164$ and $p/p_o = 0.260$, therefore, increasing α changes the position of the dome. It is worth noting that the trajectory of the dome curve for $\alpha = 11.01°$ is shown in Figure 4, where the curves from the numerical simulations are superimposed on the experimental pressure data [5].

Figure 10. Static pressure patterns at the nozzle wall, for (a) $\boldsymbol{\alpha = 9°}$, (b) $\boldsymbol{\alpha = 11.01°}$ and (c) $\boldsymbol{\alpha = 13°}$

Flow Field: Static Temperature

The static temperature distribution in the flow field is shown in Figure 11(a) for $\alpha = 9°$, Figure 11(b) for $\alpha = 11.01°$ and Figure 11(c) for $\alpha = 13°$. For NPR $= 2.412$, at the shock position, the region with the lowest temperature drop is observed. For NPR$=3.413$, the region with the lowest temperature drop is at the exit of the nozzle where the shock wave occurs. While, for NPR $= 5.423$ and NPR $= 8.78$ the propagation of the temperature drops is presented up to the region of the atmosphere, being with greater intensity for NPR $= 8.78$.

Figures 12(a), 12(b) and 12(c) shows the static temperature patterns evaluated in the symmetry in the nozzle and atmosphere section. For the shock wave occurring inside the nozzle for NPR $= 2.412$, it is observed that for $\alpha = 9°$ the shock position is located at $x/x_t = 1.74$ and with temperature drop $T/T_o = 0.614$; for $\alpha = 11.01°$ the shock position is located at $x/x_t = 1.7$ and with temperature drop $T/T_o = 0.594$; as well as, for $\alpha = 13°$ the shock position is located at $x/x_t = 1.67$ and with temperature drop $T/T_o = 0.563$. Therefore, the increase of α allows an increase of temperature drop of the flow inside the nozzle. For NPR $= 2.412$, the temperature profile of the flow in the atmosphere tends to have a horizontal trajectory behaviour, as well as the pressure and the flow velocity. For NPR $= 3.413$, NPR $= 5.413$ and NPR $= 8.78$, temperature fluctuations occur in the atmosphere. At the nozzle outlet at position $x/x_t = 2$, for NPR $= 3.413$, NPR $= 5.423$ and NPR $= 8.78$, for $\alpha = 9°$ the flow reaches the temperature drop $T/T_o = 0.574$, for $\alpha = 11.01°$ the temperature drop $T/T_o = 0.555$ and for $\alpha = 13°$ the temperature drop $T/T_o = 0.535$. Therefore, in symmetry, at the exit of the nozzle, for $\alpha = 9°$ the static temperature has the magnitude of 169.01 K, for $\alpha = 11.01°$ the magnitude of 163.41 K, and for $\alpha = 13°$ the magnitude of 157.52 K, respectively.
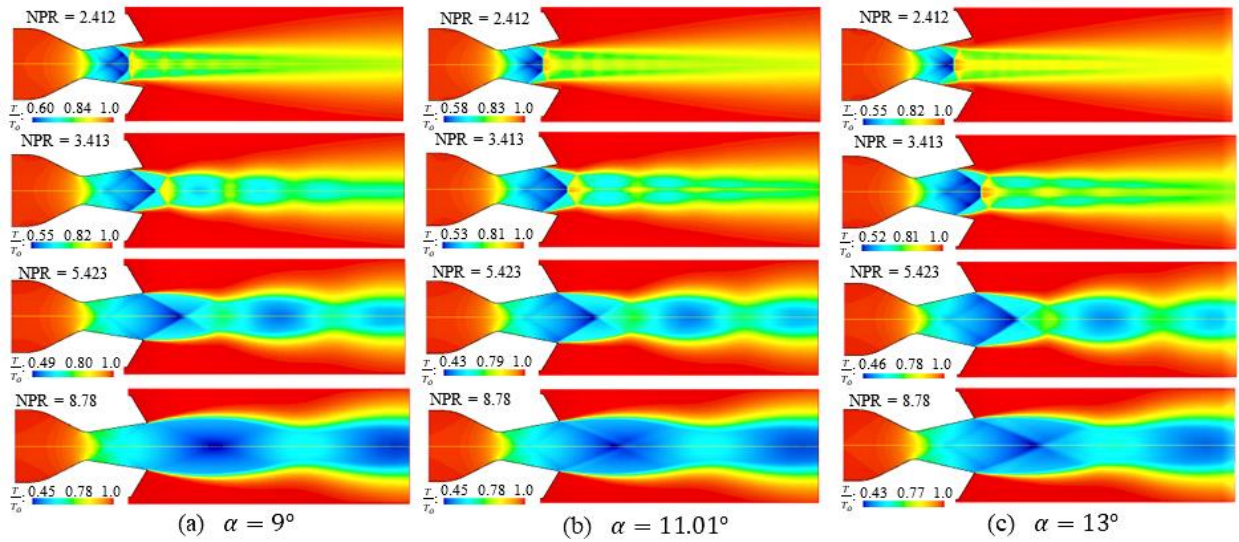
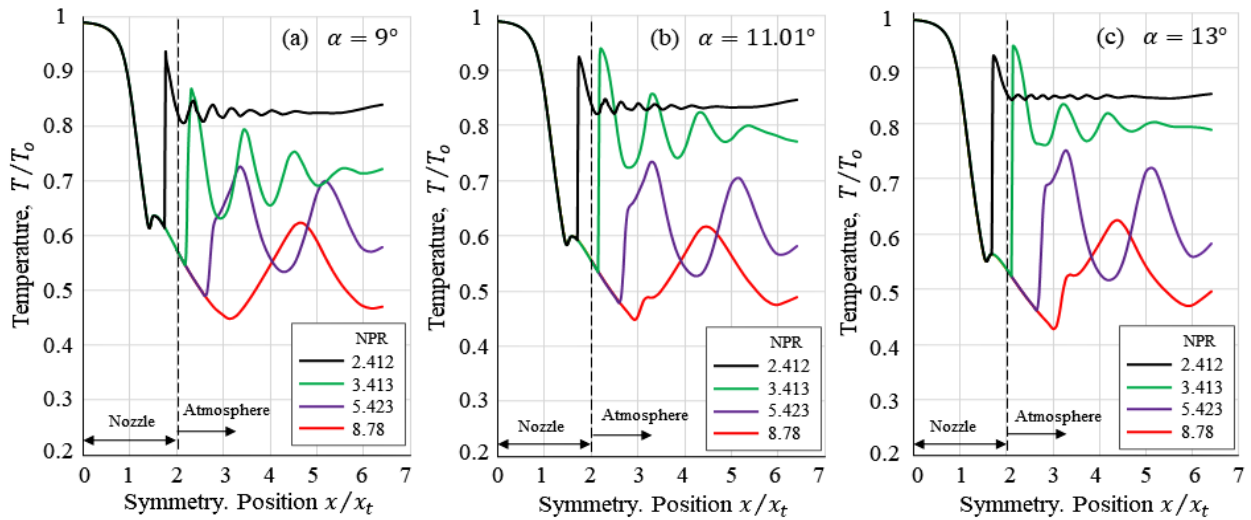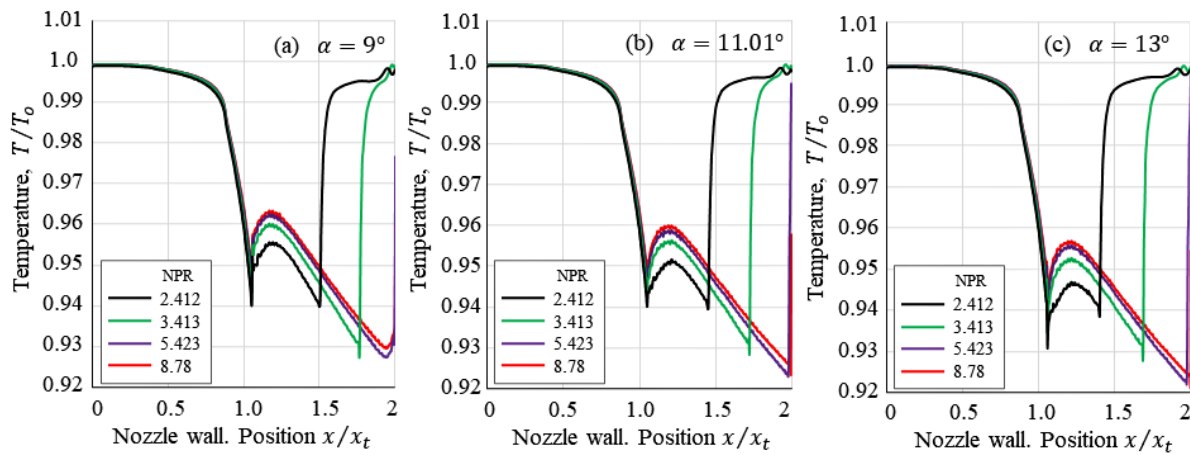**Figure 11.** Flow field: static temperature, for (a) $\alpha = 9°$, (b) $\alpha = 11.01°$ and (c) $\alpha = 13°$

Figure 12. Static temperature patterns in symmetry, for (a) $\alpha = 9°$, (b) $\alpha = 11.01°$ and (c) $\alpha = 13°$

The static temperature patterns at the adiabatic nozzle wall have a different behaviour from the flow region in the nozzle symmetry, both in the converging and diverging section, as shown in Figures 13(a), 13(b) and 13(c). It is observed that the divergent wall is heated by flow friction in the region of the thermal boundary layer thickness, and the exchange of the amount of molecule motion and heat transfer are small enough that they do not heat the nozzle walls sufficiently to account for the thermal effect on adiabatic walls. However, the wall temperature due to flow friction reaches temperatures above the central region of the flow. In addition, it shows in which regions the maximum and minimum temperatures occur.

When considering a viscous flow model in the computational domains, the thermal boundary layer adjacent to the wall is considered. In the region of the thermal boundary layer the process is irreversible, so it is not considered in that thin layer as an isentropic process, so the temperature patterns shown in Figure 13 are obtained. It is observed that the temperature profiles unify at the nozzle outlet, with a tendency to reach the ambient temperature of the atmosphere. This is due to the fact that between the flow separation section and the nozzle exit there is a pressure lower than the pressure of the atmosphere, so that the flow from the atmosphere is induced to enter by brushing the adiabatic wall until the proximity of the flow separation, at the same time there is recirculation of the flow to exit together with the supersonic jet, as shown in the velocity field with respect to the Mach number in Figures 6(a), 6(b) and 6(c).

Figure 13. Static temperature patterns at the nozzle wall, for (a) $\alpha = 9°$, (b) $\alpha = 11.01°$ and (c) $\alpha = 13°$

The behaviour of the flow in the velocity field is based on the relationships of thermodynamic parameters, such as density, pressure and temperature, expressed in the equation of state of ideal gases. Therefore, any variation of some of these parameters in some region of the flow causes the Mach number to change, whether at subsonic, transonic or supersonic velocity. In addition, the effect of increasing α causes the flow to condition during expansion, varying the density of the flow, as well as the structure of the internal shocks. For NPR = 2.412 and NPR = 3.413, the internal shocks for the Mach number, static pressure and static temperature fields are similar to the internal shocks reported by Hunter [5], which are shown in Figure 5. In the region where the intersection of the internal shocks is located, there is a fluctuation, so the flow in that region has variations of magnitudes of the thermodynamic parameters, and the distance between the shock wave and the fluctuation shortens as α increases. Where, for $\alpha = 9°$ (Figures 7(a), 9(a) and 12(a)) the fluctuation is located at the estimated position $x/x_t = 1.4$, for $\alpha = 11.01°$ (Figures 7(b), 9(b) and 12(b)) at the estimated position $x/x_t = 1.48$, and for $\alpha = 13°$ (Figures 7(c), 9(c) and 12(c)) at the estimated position $x/x_t = 1.56$, respectively.

Studies for hot flow in 2D computational domains for conical nozzle geometries for $\alpha < 12°$, reported internal shocks [34-37], where in the intersection region of the shocks, the Mach number variations have a larger fluctuation. Therefore, the planar nozzle having a rectangular cross section, the flow behaviour has differences with respect to the conical nozzles having a circular cross section, where, the flow expansion in the divergent in a planar nozzle will be different with respect to a conical nozzle. In addition, the effect that the four walls of the planar nozzle have on the pressure gradients, temperature, Mach number and density will be different between cold and hot flow.

CONCLUSION

On the basis of the analyses carried out, it is concluded:

- The Mach number, static pressure and static temperature evaluated in the symmetry, for $\alpha = 9°$, $\alpha = 11.01°$ and $\alpha = 13°$; it is found that for $\alpha = 13°$ the flow velocity presents a slight increase in acceleration at the exit of the nozzle at the position $x/x_t = 2$, besides presenting the lowest pressure drop and temperature, this is for NPR = 3.413, NPR = 5.413 and NPR = 8.78. Where, for $\alpha = 9°$ the flow reaches the estimated value of Mach number 1.92, for $\alpha = 11.01°$ the Mach number 2.00 and for $\alpha = 13°$ the Mach number 2.084. Therefore, with respect to the nozzle with $\alpha = 11.01°$ taken as reference, for $\alpha = 13°$ there is an increase in velocity of 4.15% and for $\alpha = 9°$ a decrease in velocity of 3.78%.

- At the wall of the adiabatic nozzle, the static temperature is increased due to the effect of the flow friction in the thermal boundary layer region, and its magnitude is much higher with respect to the static temperature in the central region of the flow. At the nozzle exit, for NPR = 3.413, NPR = 5.423 and NPR = 8.78, in the central region of the flow, for $\alpha = 9°$ the flow reaches the static temperature of magnitude 169.01 K, for $\alpha = 11.01°$ the magnitude of 163.41 K and for $\alpha = 13°$ the magnitude of 157.52 K, respectively.

- For future research, the study of the flow field in symmetric planar nozzles in computational domains should be extended for other pressure and temperature magnitudes, as well as increasing the divergence length, in order to obtain more information on the compressible flow regimes, on the flow turbulence and propagation of internal shocks for 2D and 3D computational domains, and the effect of gravity should be considered for the flow discharge in the atmosphere region in 3D domains.

ACKNOWLEDGEMENT

REFERENCES

[1]   G. P. Sutton, and O. Biblarz, *Rocket Propulsion Elements*. John Wiley and Sons, New York, 2016.

[2]   H. Schlichting, and K. Gersten, *Boundary-layer Theory*, Berlin Heidelberg, Germany, Springer Verlag, 9th ed., 2017.

[3]   T. V. Karman, "The fundamentals of the statistical theory of turbulence," *Journal of the Aeronautical Sciences*, vol. 4, no. 4, pp. 131–138, 1937.

[4]   J. D. Anderson, *Fundamentals of Aerodynamics*, McGraw-Hill Education, New York, 2017.

[5]   C. A. Hunter, "Experimental, theoretical, and computational investigation of separated nozzle flows," in *34th AIAA/ASME/SAE/ASEE Joint Propulsion Conference* & Exhibit, Cleveland, OH, USA, 1998.

[6]   C. Génin, and R. Stark, "Hot flow testing of dual bell nozzles," in *49th AIAA Aerospace Sciences Meeting Including the New Horizons Forum and Aerospace Exposition,* Orlando, Florida, 2011.

[7]   J. Östlund, and B. Muhammad-Klingmann, "Supersonic flow separation with application to rocket engine nozzles," *Applied Mechanics Reviews,* vol. 58, no. 3, pp. 143-177, 2005.

[8]   S. Ristić, M. Kozić, and M. Puharić, "Experimental and numerical investigation of flow separation in a supersonic nozzle," *Journal of Russian Laser Research,* vol 29, no. 4, pp. 377–389, 2008.

[9]   L. Li, and T. Saito, "Numerical and experimental investigations of fluidic thrust vectoring mechanism," *International Journal of Aerospace Innovations,* vol. 4, pp. 53–64, 2012.

[10]   M. Sajben, T. Bogar, and J. Kroutil, "Forced oscillation experiments in supercritical diffuser flows with application to ramjet instabilities," in *17th Joint Propulsion Conference,* Colorado Springs, USA, pp.1-12, 1981.

[11]   P. Krehl and S. Engemann, "August toepler —the first who visualized shock waves," *Shock Waves*, vol. 5, no. 1, pp. 1–18, 1995.

[12]   A. Shapiro, *The Dynamics and Thermodynamics of Compressible Fluid Flow,* John Wiley and Sons, vol. I, 1953.

[13]   J. Blazek, *Computational Fluid Dynamics: Principles and Applications*, Oxford, United Kingdom: Butterworth-Heinemann, 2015.

[14]   D. C. Wilcox, *Turbulence Modeling for CFD*, DCW Industries, California, USA, 2006.

[15]   A. Balabel, A. M. Hegab, M. Nasr, and S. M. El-Behery, "Assessment of turbulence modeling for gas flow in two dimensional convergent–divergent rocket nozzle," *Applied Mathematical Modelling*, vol. 35, no. 7, pp. 3408–3422, 2011.

[16]   S. L. Tolentino, "Evaluation of turbulence models for the air flow in a planar nozzle," *INGENIUS*, no. 22, pp. 25–37, 2019.

[17]   A. B. M. Toufique Hasan, "Characteristics of overexpanded nozzle flows in imposed oscillating condition," *International Journal of Heat and Fluid Flow*, vol. 46, pp. 70–83, 2014.

[18]   V. M. K. Kotteda and S. Mittal, "Flow in a planar convergent–divergent nozzle," *Shock Waves*, vol. 27, no. 3, pp. 441–455, May 2017.

[19]   S. Asbury, C. Gunther, and C. Hunter, "A passive cavity concept for improving the off-design performance of fixed-geometry exhaust nozzles," in *32nd Joint Propulsion Conference and Exhibit.* Florida, USA, pp. 1-31, 1996.

[20]   J. A. Owczarek, and D. O. Rockwell, "An experimental study of flows in planar nozzles," *Journal of Basic Engineering,* vol. 94, no. 3, pp. 682-688, 1972.

[21]   A. Bourgoing, and P. Reijasse, "Experimental analysis of unsteady separated flows in a supersonic planar nozzle," *Shock Waves,* vol 14, no. 4, pp. 251–258, 2005.

[22]   D. Papamoschou, and A. Zill, "Fundamental Investigation of Supersonic Nozzle Flow Separation," *42nd AIAA Aerospace Sciences Meeting and Exhibit.* pp.1-17, january 5-8, 2004.

[23]   S. B. Verma, and C. Manisankar, "Origin of flow asymmetry in planar nozzles with separation," *Shock Waves,* vol. 24, no. 2, pp. 191–209, 2014, doi: 10.1007/s00193-013-0492-1.

[24]   R. Arora, and A. Vaidyanathan, "Experimental investigation of flow through planar double divergent nozzles," *Acta Astronautica,* vol. 112, pp. 200–216, 2015.

[25]   O. Kostić, Z. A. Stefanović, and I. A. Kostić, "CFD modeling of supersonic airflow generated by 2D nozzle with and without an obstacle at the exit section," *FME Transaction*s, vol. 43, no. 2, pp. 107-113, 2015.

[26]   B. Wagner, R. Stark, and S. Schlechtriem, "Experimental study of a planar expansion deflection nozzle," *Progress in Propulsion Physics*, vol. 2, pp. 641-654, 2011.

[27]   P. P. Nair, A. Suryan, and H. D. Kim, "Computational study on reducing flow asymmetry in over-expanded planar nozzle by incorporating double divergence," *Aerospace Science and Technology,* vol. 100, p. 105790, 2020.

[28]   ANSYS, "Ansys Fluent 12.0 Documentation," Theory guide [Online], 2022, Available: https://www.afs.enea.it/project/neptunius/docs/fluent.

[29]   P. R. Spalart, and S. R. Allmaras, "A one-equation turbulence model for aerodynamic flows," in *30th Aerospace Sciences Meeting and Exhibit,* Reno, NV, U.S.A, pp. 1-22, 1992.

[30]   W. Sutherland, "LII. The viscosity of gases and molecular force," *Magazine and Journal of Science,* vol. 36, no. 223, pp. 507–531, 1893.

[31]   D. C. Wilcox, "Reassessment of the scale determining equation for advanced turbulence models," *AIAA Journal*, vol. 26, no. 11, pp. 1299–1310, 1988.

[32] F. R. Menter, "Two-equation eddy-viscosity turbulence models for engineering applications," *AIAA Journal,* vol. 32, no. 8, pp. 1598–1605, 1994.

[33] B. E. Launder, G. J. Reece, and W. Rodi, "Progress in the development of a Reynolds-stress turbulence closure," *Journal of Fluid Mechanics,* vol. 68, no. 3, pp. 537-566, 1975.

[34] S. L. Tolentino, and J. Mírez, "Numerical analysis of over-expanded flow in the experimental ULA-2 conical nozzle out of design," *Lámpsakos*, vol. 2020, no. 24, pp. 33-47, 2020 (*in Spanish*).

[35] S. L. Tolentino, M. A. Parco, S. Caraballo, L. Lacruz, V. Marcano, J. Ferreira, and J. Mírez, "Numerical analysis of the flow behavior in the throat section of an experimental conical nozzle," *Enfoque UTE*, vol. 12, no. 1, pp. 12–28, 2021 (*in Spanish*).

[36] S. L. Tolentino, and O. González, "Numerical analysis of the over-expanded flow in the experimental conical nozzle ULA-1B out of design," *Lámpsakos*, vol. 2021, no. 24, pp. 33-47, 2021 (*in Spanish*).

[37] S. L. Tolentino, and J. Mírez, "Throat length effect on the flow patterns in off-design conical nozzles," *FME Transactions*, vol. 50, no. 2, pp. 271-282, 2022.